Monthly Notices
of the
ROYAL ASTRONOMICAL SOCIETY

MNRAS **534,** 271–280 (2024) https://doi.org/10.1093/mnras/stae2012
Advance Access publication 2024 August 31

The progenitor star of SN 2023ixf: a massive red supergiant with enhanced, episodic pre-supernova mass loss

Yu-Jing Qin ,[1★] Keming Zhang ,[2,3] Joshua Bloom,[2] Jesper Sollerman ,[4] Erez A. Zimmerman ,[5] Ido Irani,[5] Steve Schulze ,[4,6] Avishay Gal-Yam,[5] Mansi Kasliwal ,[1] Michael W. Coughlin,[7] Daniel A. Perley ,[8] Christoffer Fremling[1,9] and Shrinivas Kulkarni[1]

[1] *Division of Physics, Mathematics and Astronomy, California Institute of Technology, 1200 E California Blvd., Pasadena, CA 91125, USA*
[2] *Department of Astronomy, University of California, Berkeley, 501 Campbell Hall 3411, Berkeley, CA 94720-3411, USA*
[3] *Department of Astronomy and Astrophysics, University of California, San Diego, 9500 Gilman Dr., La Jolla, CA 92093, USA*
[4] *Department of Astronomy, The Oskar Klein Center, Stockholm University, AlbaNova University Center, SE 106 91 Stockholm, Sweden*
[5] *Department of Particle Physics and Astrophysics, Weizmann Institute of Science, 234 Herzl Street, POB 26, Rehovot 7610001, Israel*
[6] *Center for Interdisciplinary Exploration and Research in Astrophysics (CIERA), Northwestern University, SE 1800 Sherman Ave., Evanston, IL 60201 , USA*
[7] *School of Physics and Astronomy, University of Minnesota, Twin Cities, 116 Church Street S.E., Minneapolis, MN 55455, USA*
[8] *Astrophysics Research Institute, Liverpool John Moores University, Liverpool Science Park, 146 Brownlow Hill, Liverpool L3 5RF, UK*
[9] *Caltech Optical Observatories, California Institute of Technology, 1200 E California Blvd., Pasadena, CA 91125, USA*

Accepted 2024 August 13. Received 2024 August 12; in original form 2023 September 17

ABSTRACT

We identify the progenitor star of SN 2023ixf in Messier 101 using Keck/NIRC2 adaptive optics imaging and pre-explosion *Hubble Space Telescope* (*HST*)/Advanced Camera for Surveys (ACS) images. The supernova, localized with diffraction spikes and high-precision astrometry, unambiguously coincides with a progenitor candidate of $m_{\mathrm{F814W}} = 24.87 \pm 0.05$ (AB). Given its reported infrared excess and semiregular variability, we fit a time-dependent spectral energy distribution (SED) model of a dusty red supergiant (RSG) to a combined data set of *HST* optical, ground-based near-infrared, and *Spitzer* Infrared Array Camera (IRAC) [3.6], [4.5] photometry. The progenitor resembles an RSG of $T_{\mathrm{eff}} = 3488 \pm 39$ K and $\log(L/\mathrm{L}_\odot) = 5.15 \pm 0.02$, with a 0.13 ± 0.01 dex (31.1 ± 1.7 per cent) luminosity variation at a period of $P = 1144.7 \pm 4.8$ d, obscured by a dusty envelope of $\tau = 2.92 \pm 0.02$ at $1\,\mu$m in optical depth (or $A_\mathrm{V} = 8.43 \pm 0.11$ mag). The signatures match a post-main-sequence star of $18.2^{+1.3}_{-0.6}\,\mathrm{M}_\odot$ in zero-age main-sequence mass, among the most massive SN II progenitor, with a pulsation-enhanced mass-loss rate of $\dot{M} = (4.32 \pm 0.26) \times 10^{-4}\,\mathrm{M}_\odot\,\mathrm{yr}^{-1}$. The dense and confined circumstellar material is ejected during the last episode of radial pulsation before the explosion. Notably, we find strong evidence for variations of τ or T_{eff} along with luminosity, a necessary assumption to reproduce the wavelength-dependent variability, which implies periodic dust sublimation and condensation. Given the observed SED, partial dust obscuration remains possible, but any unobstructed binary companion over $5.6\,\mathrm{M}_\odot$ can be ruled out.

Key words: stars: supergiants – supernovae: individual: SN 2023ixf – transients: supernovae.

1 INTRODUCTION

Connecting the diverse supernova (SN) phenomena to the properties and late-stage evolution of progenitor stars is a pivotal task in the study of stellar transients. Deep and high-resolution pre-explosion images of nearby host galaxies, particularly acquired with the *Hubble Space Telescope* (*HST*) over its three decades of operation, remains the only direct approach to constrain SN progenitor properties.

Currently, there are about 30 core-collapse supernovae (CCSNe) with direct progenitor detections (e.g. Smartt 2015; Van Dyk 2017) and the majority of them are Type II supernovae (SNe II), the most abundant SN subclass by volumetric rates (e.g. Li et al. 2011a; Shivvers et al. 2017). SN II progenitors retain part of their hydrogen-rich envelopes before the explosion, giving rise to Balmer emission lines in their photospheric-phase spectra. Direct progenitor detections broadly support the scenario that single massive stars with zero-age main-sequence (ZAMS) mass of about 8 to $18\,\mathrm{M}_\odot$ explode as SNe II during the red supergiant (RSG) phase (e.g. Smartt 2009, 2015) – the most well-established case of SN-progenitor connection so far, especially when considering the limited samples and heterogeneity of progenitors detected for other CCSNe subclasses (Van Dyk 2017).

Despite the success, the RSG-to-SN II connection is not yet completely understood. A major unsettled issue is that directly detected SN II progenitors are rarely more luminous than $\log(L/\mathrm{L}_\odot) \sim 5.1$ (or more massive than $\sim 18\,\mathrm{M}_\odot$), but the observed RSG population in the Milky Way and nearby galaxies extends to $\log(L/\mathrm{L}_\odot) \sim 5.5$ (or ~ 25–$30\,\mathrm{M}_\odot$), a discrepancy commonly referred to as the 'RSG problem' (Smartt 2009, 2015; but see also Davies & Beasor 2018, 2020). The absence of SN II progenitors above $\log(L/\mathrm{L}_\odot) \sim 5.1$

★ E-mail: yujingq@caltech.edu

could be attributed to the direct collapse of massive RSGs into black holes (e.g. O'Connor & Ott 2011; Horiuchi et al. 2014), the increased circumstellar extinction near massive RSGs (Walmswell & Eldridge 2012; Beasor & Davies 2016), or a 'superwind' phase that removes the hydrogen-rich envelopes and produces stripped-envelope SNe instead of SNe II (Yoon & Cantiello 2010; but see also Beasor & Smith 2022). Expanding the existing sample of directly detected SN II progenitors, determining their luminosity, ZAMS mass, and mass-loss rate, and identifying limiting cases of progenitor properties would be vital to test these possible scenarios.

The nearby SN 2023ixf in the galaxy Messier 101 provides a once-in-a-decade opportunity to take a closer look at a SN II progenitor through the rich pre-explosion data. SN 2023ixf was reported by Itagaki (2023) on 2023 May 19 at 21:42 UT and was spectroscopically classified by Perley et al. (2023). Early spectroscopic follow-up campaign focuses on the dense and confined circumstellar material (CSM) probed by flash ionizing features in the optical and ultraviolet wavelengths (Bostroem et al. 2023; Hiramatsu et al. 2023; Jacobson-Galán et al. 2023; Smith et al. 2023; Teja et al. 2023; Vasylyev et al. 2023; Yamanaka, Fujii & Nagayama 2023; Zimmerman et al. 2024); both spectropolarimetry (Vasylyev et al. 2023) and high-resolution spectroscopy (Smith et al. 2023) suggest asymmetric CSM distribution. Photometric analyses (Hiramatsu et al. 2023; Hosseinzadeh et al. 2023; Jacobson-Galán et al. 2023; Teja et al. 2023; Zimmerman et al. 2024) also require CSM interaction as an additional power source of SN emission, and it has been suggested that the dense and confined CSM leads to an extended shock breakout phase (Hiramatsu et al. 2023; Hosseinzadeh et al. 2023; Zimmerman et al. 2024). The shock–CSM interaction is detected in soft X-ray (Panjkov et al. 2023; Chandra et al. 2024), and notably, early in hard X-ray (Grefenstette et al. 2023). As a bright nearby SN, small telescope arrays (Bianciardi et al. 2023; Sgro et al. 2023) and amateur astronomers (Mao et al. 2023; Yaron et al. 2023) have contributed valuable early-time data of SN 2023ixf. In particular, the early-time multicolour light curve from amateur data reveals dramatic colour evolution over the span of just a few hours, hinting at the disruption of dust near the progenitor (Li et al. 2024). Furthermore, the absence of submillimetre (Berger et al. 2023), gamma-ray (Ravensburg et al. 2024; Sarmah 2024), and neutrino (Guetta et al. 2023; Sarmah 2024) detections at early time also impose constraints on the progenitor properties and the detailed physical processes of CCSNe.

Finally, the physical properties of a candidate progenitor star have been discussed in several recent papers (Jencson et al. 2023; Kilpatrick et al. 2023; Niu et al. 2023; Pledger & Shara 2023; Soraisam et al. 2023; Van Dyk et al. 2024; Xiang et al. 2024). The red optical colour, strong infrared excess, and semiregular variability of the candidate indicate a luminous RSG with radial pulsations, heavily obscured by circumstellar dust. Retrospective analysis of archival optical (Dong et al. 2023; Panjkov et al. 2023; Neustadt, Kochanek & Smith 2024; Ransome et al. 2024), ultraviolet (Flinner et al. 2023; Panjkov et al. 2023), and X-ray (Panjkov et al. 2023) data rules out bright outbursts and eruptive mass loss of the candidate.

In this work, we localize the progenitor star of SN 2023ixf using high-resolution adaptive optics imaging. We also constrain its progenitor properties by fitting pre-explosion photometry with the SED of a dusty RSG. We confirm and strengthen the identification of the progenitor in previous works and demonstrate that the progenitor is close to the empirical luminosity upper limit of SN II progenitors. Through the paper, we use a distance to the host of $D = 6.90 \pm 0.12$ Mpc (or $\mu = 29.194 \pm 0.039$ in distance modulus; Riess et al. 2022), and luminosity values are calculated with distance uncertainty folded in. Source brightness, if in magnitude scale, is reported in the AB magnitude system.

2 DATA

2.1 Pre-explosion *HST* observations

The SN location has been imaged by several *HST* programs before the explosion, including proposal IDs 6829 (PI: You-Hua Chu), 9490 (PI: Kip Kuntz), 9720 (PI: Rupali Chandar), 13361 (PI: William Blair), and 15192 (PI: Benjamin Shappee), with a variety of instrument and band combinations, covering a time frame of nearly three decades.

We access the calibrated science images from these programs at the Mikulski Archive for Space Telescopes.[1] The data archive also provides single-visit mosaics for the Wide Field Camera 3 (WFC3) and Advanced Camera for Surveys (ACS) programs. We choose the stacked image from proposal ID 9490, which combines 2340 s of exposure in the *F435W*, *F555W*, and *F814W* bands and are aligned with *Gaia* sources (Gaia Collaboration 2018), as our detection image and astrometric reference frame (Fig. 1, left panel). Due to the limited pointing repeatability of *HST*, we also register calibrated science images to this reference image using `TweakReg` in DRIZZLEPAC[2] so they share the same astrometric reference frame and can be used for forced point spread function (PSF) photometry later.

2.2 Adaptive optics imaging with Keck/NIRC2

We imaged the field of SN 2023ixf on 2023 May 25 at 11:16 UT (6.6 d after the explosion) using the Near-Infrared Camera (NIRC2) with Natural-Guide-Star Adaptive Optics (AO) on the W. M. Keck II telescope, under program ID U152 (PIs: Bloom, Zhang). To increase the overlap with the pre-explosion *HST*/ACS image and hence the number of usable astrometric reference stars, we choose the wide camera mode (40 arcsec square field, 0.0397 arcsec pixel^{-1}). We acquired three 60-s science images in the *K*-short (*Ks*) band and an additional 60-s image at a nearby empty field for sky background and dark current subtraction. The science images are then sky-subtracted, flat-corrected, and averaged into a single image. We also create a per-pixel uncertainty map with `calc_total_error` implemented in PHOTUTILS (Bradley et al. 2022), using the instrument gain. The observing setup here allows us to detect fainter astrometric reference stars, but the SN itself becomes inevitably saturated due to the dramatic contrast in brightness between the SN and other stars in the field. We localize the SN with diffraction spikes, as described in the next section.

2.3 Infrared photometry from the literature

Messier 101, the host galaxy of SN 2023ixf, has been continuously monitored by the *Spitzer Space Telescope* over the past two decades. Retrospective analysis of archival *Spitzer*/IRAC data at the SN position revealed the semiregular variability of a likely progenitor in the [3.6] and [4.5] bands (Jencson et al. 2023; Kilpatrick et al. 2023; Soraisam et al. 2023; hereafter J23, K23, S23), with an amplitude of 70 per cent (K23) and a period of about 1100 d (J23, S23). The *Spitzer* source is coincident with the best-localized SN position based on our high-resolution Keck/NIRC2 image. To constrain the stellar

---

[1] https://archive.stsci.edu/

[2] https://github.com/spacetelescope/drizzlepac

and CSM properties of the progenitor, we obtain the *Spitzer*/IRAC measurements in J23. The reported Vega magnitudes are converted to flux densities (in μJy) based on the zero-magnitude fluxes in the IRAC Instrument Handbook.[3] Since the source is undetected in the *Spitzer*/IRAC [5.8] and [8.0] bands and only flux upper limits are reported in the literature, we have excluded these bands in our SED modelling to maintain methodological consistency. Notably, the measured *Spitzer*/IRAC fluxes vary across independent analyses, which may be attributed to different data sources and methodologies employed, as discussed in S23 and Van Dyk et al. (2024).

The source is also detected in archival ground-based near-infrared (NIR) images (J23, K23, S23), which reveal similar variability (J23, S23) with a potentially greater amplitude than in the *Spitzer*/IRAC bands (S23). For our analysis, we compiled NIR magnitudes from several sources: (1) one epoch of *K*-band magnitudes in S23, based on the Gemini Near-Infrared Imager (NIRI) data; (2) one epoch of *Ks*-band magnitude in K23, based on the Mayall 4-m Telescope NOAO Extremely Wide Field Infrared Imager data; (3) eight epochs of *J*-, *H*-, and *K*-band magnitudes in S23, based on the archival data of UKIRT Wide Field Camera; and (4) five epochs of *J*- and *Ks*-band magnitudes in J23, based on the MMT and Magellan Infrared Spectrograph (MMIRS) data. The reported magnitudes are also converted to flux densities. We choose the zero magnitude flux densities of the Two Micron All Sky Survey (2MASS; Skrutskie et al. 2006) since the reported Vega magnitudes are calibrated with 2MASS sources. We also note that K23 measured a fainter NIRI *K*-band magnitude than S23, which could be due to the different methods applied. We choose the NIRI magnitude from S23 for our analysis.

3 ANALYSIS AND RESULTS

3.1 Astrometric localization

To identify the progenitor star in the pre-explosion *HST*/ACS image, we first locate the exact pixel position of the SN in the Keck/NIRC2 image, and then transform the pixel position to the *HST*/ACS image.

Given that the SN is saturated, we localize its pixel position using the diffraction pattern caused by the hexagonal mirror segments (Fig. 2, left). Since the primary is symmetric, the instrument is on-axis, and the field is centred at the SN, the spikes should intersect at the SN location. To determine the *X*-axis positions of the north–south spike and *Y*-axis positions of the northeast–southwest and northwest–southeast spikes, we extract 1D light profiles and the associated uncertainty along adjacent horizontal or vertical slices with a width of 10 pixel, then fit the 1D light profiles with a Gaussian component on a linear background. The peak of the Gaussian component and the uncertainty represent the spike position along the slice. Erroneously determined spike positions, due to either the absence of a peak or the existence of other sources, are removed during visual inspection. We fit the remaining 54 spike positions using three lines separated by 60° sharing a common intersection point. The free parameters are the central position (x_c, y_c) and the position angle (θ) of the entire pattern. We use EMCEE (Foreman-Mackey et al. 2013), a Markov Chain Monte Carlo (MCMC) sampler, to carry out the fit. Upon convergence, the SN position in the Keck/NIRC2 image is determined down to a statistical error (geometric mean of uncertainties in x_c and y_c) of 0.04 pixel or 1.6 mas.

We then fit a relative astrometric solution across Keck/NIRC2 and *HST*/ACS images to transform the SN position back onto the pre-explosion image. First, we detect point sources above a signal-to-noise ratio (SNR) threshold of 5 in the Keck/NIRC2 image and 10 in the *HST*/ACS image, with the DAOFIND algorithm implemented in PHOTUTILS (Bradley et al. 2022). Within 15 arcsec from the SN position, we choose 31 unambiguous and isolated point sources in the Keck/NIRC2 image that are also detected in the *HST*/ACS image as reference stars. The astrometric solution is obtained by fine-tuning the central RA/Dec., orientation, and pixel scale of the Keck/NIRC2 image so the predicted pixel position of reference stars, based on the measured sky coordinates in the *HST*/ACS image and the fine-tuned World Coordinate System parameters, best matches their detected positions. The transformation parameters are estimated using EMCEE, where the inverse variance-weighted sum of squared residual distances is minimized. Upon convergence, the central coordinate of the Keck/NIRC2 image is determined down to an uncertainty of 5.6 mas, which we consider the statistical error of the astrometric solution. For the eight nearest reference stars within 7.3 arcsec to the SN position, the mean residual error of the astrometric solution is 18.6 mas, which we consider the systematic error of the astrometric solution. As a cross-check, we also fit an Affine transformation of pixel positions across Keck/NIRC2 and *HST*/ACS images including translation, rotation, and scaling, with the same set of reference stars. We obtain consistent central coordinates within the statistical errors.

The SN position localized by fitting diffraction spikes, after transformed to the pre-explosion colour-composite *HST*/ACS image, points to a red source (Fig. 1) with a total uncertainty of 19.5 mas. The red source is also the most likely progenitor candidate proposed in earlier works, including the localization by Van Dyk et al. (2024) using ’Alopeke imaging.

3.2 Progenitor identification and forced photometry

To confirm the spatial coincidence of SN 2023ixf with the red source in the pre-explosion *HST*/ACS colour-composite image, we first identify sources in the three-band combined *HST*/ACS image. We use the iteratively subtracted PSF photometry technique, which is optimized for crowded-field photometry, for this purpose. First, inside a radius of 20 arcsec to the SN, we choose 45 relatively isolated, high SNR stars and construct an effective PSF (EPSF) using `EPSFBulder` in PHOTUTILS. We then identify point-like sources with DAOFIND, fit sources with the PSF, and subtract the best-fitting PSF from the image. The residual image is then used for another round of source detection and subtraction, and newly detected sources are fit together with sources detected in previous rounds. We repeat this procedure until no new source is detectable in the residual image at an SNR threshold of 2. Based on the residual images, the sensitivity limit of the source detection procedure is better than $m_{\mathrm{F435W}} \simeq 27.4$, $m_{\mathrm{F555W}} \simeq 27.0$, and $m_{\mathrm{F814W}} \simeq 27.4$, assuming that the three-band combined image increases the sensitivity.

The red source is detected at a high SNR of 15.9 with a position uncertainty of 3.3 mas. The distance of the SN to this source is 12.7 ± 19.8 mas, consistent with spatial coincidence. There is another fainter source near the red source detected at a SNR of 6.7 during the second round of iteration, with a position uncertainty of 10.3 mas. The distance of this source to the SN is 128.9 ± 22.1 mas, which clearly rules out the possibility of spatial coincidence. Based on the distances, we believe that the red source is the progenitor of SN 2023ixf. We confirm the progenitor candidate identified in earlier works (e.g. Pledger & Shara 2023, K23; Van Dyk et al. 2024) with a substantially improved level of accuracy. However, it should be emphasized that although AO imaging provides angular resolution

---

[3] https://irsa.ipac.caltech.edu/data/SPITZER/docs/irac/

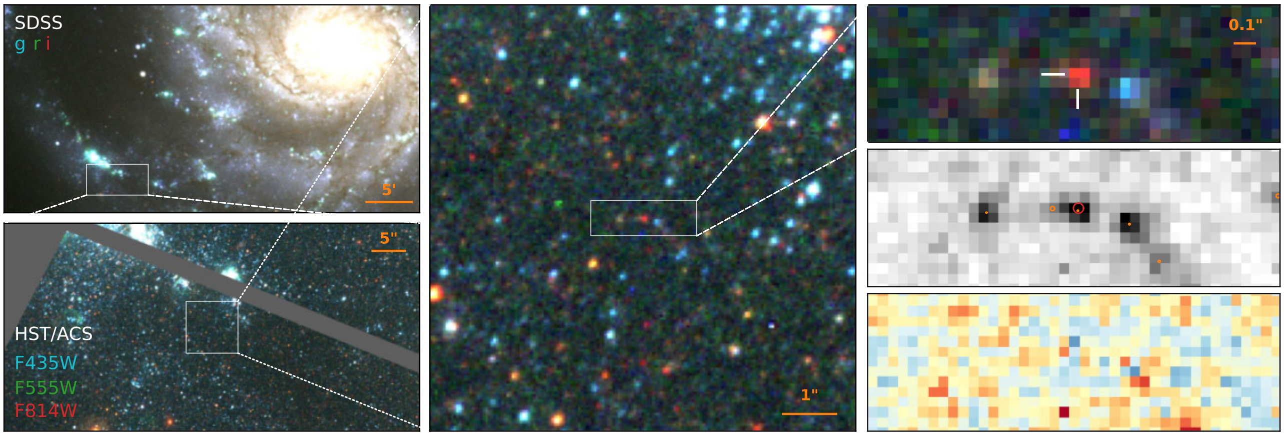

Figure 1. The progenitor star of SN 2023ixf in its host galaxy, Messier 101. The upper left panel shows a Sloan Digital Sky Survey (SDSS) cutout, and the following zoom-in panels show the *HST*/ACS colour-composite image near the SN. The upper right panel indicates the SN position localized with Keck/NIRC2 adaptive optics image. The middle panel shows the sources detected in the pre-explosion *HST*/ACS image with smaller, light circles showing the 1σ error of source positions, and the large, dark circle indicating our Keck/NIRC2 localization error (including systematic error). Finally, the lower right panel shows the residual map (-3 to 3 times the background RMS) after the source detection procedure. The SN position localized with our Keck/NIRC2 image unambiguously coincides with the red source indicated by the cross hair in the upper right panel.

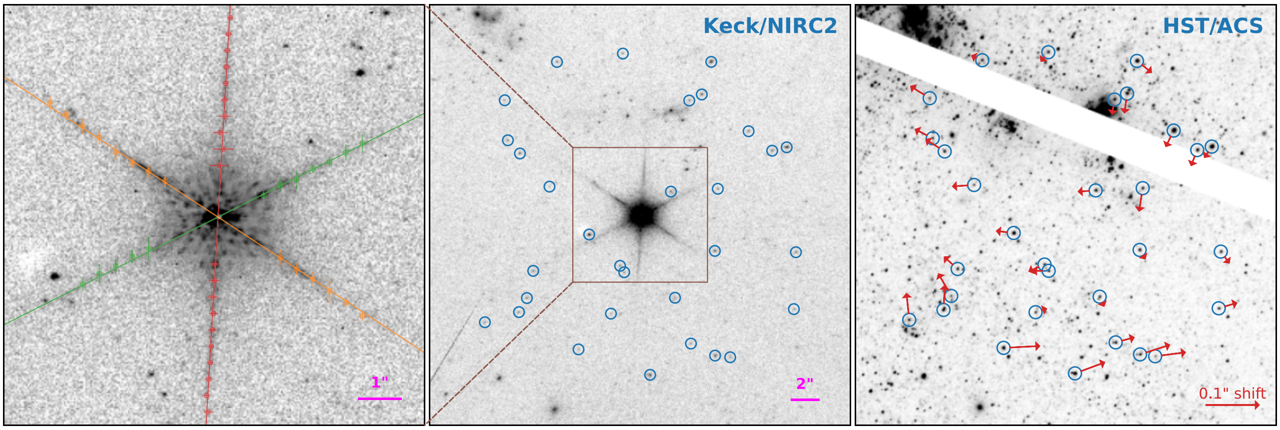

Figure 2. Localizing SN 2023ixf in the pre-explosion *HST*/ACS image using Keck/NIRC2 adaptive optics imaging. The left panel shows a contrast-enhanced cutout of the post-explosion Keck/NIRC2 *Ks*-band image (middle panel, in north-up, east-left orientation), centred at the heavily saturated SN. The SN location is precisely determined by fitting the positions of diffraction spikes (data points with error bars) using a simple linear pattern (lines). The middle panel shows the astrometric reference stars (circles) detected in the Keck/NIRC2 image, while the right panel shows the same field of the three-band combined *HST*/ACS image. Fitting an astrometric solution with these stars, the SN can be localized with a total uncertainty of 19.5 mas in the *HST*/ACS image. Arrows indicate the residual error of the best-fitting astrometric solution, which dominates the error budget.

comparable to that of *HST*, the systematics, particularly the distortion pattern of the focal plane, might be the limiting factor in the accuracy. Future *HST* imaging could provide further validation of current localization efforts, especially through the final disappearance of the candidate once the SN has faded (e.g. Van Dyk et al. 2023).

Since the progenitor resides in a relatively crowded field with a non-smooth background contributed by unresolved sources, we use forced PSF photometry to measure the source flux in the calibrated science images (rather than drizzled mosaics), with pixel area map and charge transfer efficiency corrections applied, if available. We choose the EPSF models of Anderson & King (2000, 2006) and Bellini, Anderson & Grogin (2018), linearly interpolated at the detector position of the progenitor. For focus position-dependent EPSF models, we choose the focal distance that best minimizes the median flux uncertainty of the sources. In case no EPSF is provided for a specific filter, we choose the one with the nearest pivotal wavelength for the same instrument. We make 12 arcsec square cutouts centred at the progenitor and place EPSF models at the source positions detected earlier, including those that are not identified as the progenitor. The source fluxes are fitted as free parameters with their positions fixed; the local background is estimated using `MMMBackground` in PHOTUTILS; and the photometric calibration is based on the zero-points in the FITS header. We calculate the inverse variance-weighted average source flux for each unique combination of instrument, filter, and epoch of observation. The averaged flux values are corrected for extinction assuming a Galactic reddening of $E(B-V)_{\rm MW} = 0.008$ mag (Schlegel, Finkbeiner & Davis 1998; Schlafly & Finkbeiner 2011), host galaxy reddening of $E(B-V)_{\rm host} = 0.031$ mag (Smith et al. 2023), and the extinction coefficients of Schlafly & Finkbeiner (2011) with $R_{\rm V} = 3.1$. The measured flux and magnitude (or 2σ limiting magnitude) are summarized in Table 1. Limiting magnitudes are derived by

Table 1. Forced PSF photometry of the progenitor in archival *HST* images.

Filter	MJD	Exposure (s)	Flux (μJy)	Magnitude[a]
	Prop. ID 6829 (PI: You-Hua Chu), WFPC2			
F656N	51345.99	1200	0.259±11.790	> 20.47
F547M	51346.06	1000	0.136±0.367	> 24.24
F656N	51260.98	1360	−0.466±4.292	> 21.57
F675W	51261.05	900	0.147±0.060	$25.98^{+0.57}_{-0.37}$
F547M	51261.15	1400	−0.012±0.063	> 26.14
	Prop. ID 9490 (PI: Kip Kuntz), ACS/WFC			
F435W	52594.00	900	0.010±0.012	> 27.96
F555W	52594.01	720	0.006±0.015	> 27.74
F814W	52594.02	720	0.409±0.018	$24.87^{+0.05}_{-0.05}$
	Prop. ID 9720 (PI: Rupali Chandar), WFPC2			
F336W	52878.33	2400	0.108±1.000	> 23.15
	Prop. ID 9720 (PI: Rupali Chandar), ACS/WFC			
F658N	53045.01	2440	0.109±0.059	> 26.22
	Prop. ID 13 361 (PI: William Blair), WFC3/UVIS			
F502N	56735.86	1310	0.161±0.121	> 25.44
F673N	56735.87	1310	0.193±0.090	$25.69^{+0.68}_{-0.42}$
	Prop. ID 15 192 (PI: Benjamin Shappee), ACS/WFC			
F658N	58207.54	2956	−0.188±0.083	> 25.85
F435W	58207.56	3712	0.010±0.009	> 28.27

Note.[a] In the AB magnitude system. If the SNR from forced PSF photometry is below 2, then a 2σ limit is reported instead.

converting twice the flux uncertainty from forced photometry into magnitudes.

3.3 Progenitor physical properties

To constrain the properties of the progenitor star and its CSM, we fit the SED of a variable dusty RSG to our *HST* optical and literature-compiled infrared photometry.

We generate a grid of SEDs with stellar effective temperature ($T_{\rm eff}$) and dust optical depth (τ) at 1μm as parameters. The spectrum of the central star is based on the Model Atmospheres with a Radiative and Convective Scheme (MARCS; Gustafsson et al. 2008) stellar atmosphere models. We use the spectra of a solar-abundance massive giant ($15\,{\rm M}_\odot$, $\log[g/({\rm cm\,s}^{-2})] = 0$) to cover the $T_{\rm eff}$ range of 3400–4000 K; we further extend the $T_{\rm eff}$ coverage down to 2400 K using the spectra of a $5\,{\rm M}_\odot$ star.[4] The dust optical depth covers the range of 0.001 to 50, in logarithmic spacing. The model grid includes 14 nodes along the $T_{\rm eff}$ axis and 50 nodes along the τ axis. We use DUSTY (Ivezic & Elitzur 1997) for dust radiative transfer modelling, with a similar setup as described in Villaume, Conroy & Johnson (2015), including both oxygen- and carbon-rich dust compositions. The circumstellar dust has a r^{-2} density profile, where the inner radius ($R_{\rm in}$) is related to the dust condensation temperature (fixed at 1100 K for carbon-rich and 700 K for oxygen-rich compositions) and stellar luminosity, while the ratio of the outer-to-inner radius is fixed at 10^3, representing an extended dust envelope. We normalize the output SED to unit bolometric flux for interpolation and rescaling.

We construct a model with bolometric flux (in $\log F$), stellar effective temperature ($T_{\rm eff}$), and circumstellar dust optical depth (in $\log\tau$) as free model parameters. Given the strong, semiregular variability of the progenitor (J23, K23, S23), we allow stellar and dust physical parameters ($\log F$, $T_{\rm eff}$, and $\log\tau$) to vary in a sinusoidal pattern with a regular period of P (a free model parameter) spanning the time frame of our photometric data set; the amplitude and initial phase of each parameter are also free model parameters. To calculate the flux density in a specific band and epoch of observation, we interpolate the grid based on the $T_{\rm eff}$ and $\log\tau$, scale the interpolated SED by the bolometric flux (F), and calculate the average flux density, weighted by the filter transmission profile obtained from the SVO Filter Profile Service.[5] We fit the Galactic and host extinction-corrected flux densities even in the absence of a statistically significant detection. We use EMCEE for MCMC sampling, while the best-fitting parameters are the peaks of 1D marginalized posterior distributions. The goodness of fit is evaluated by the Bayesian evidence ($\log Z$) calculated using DYNESTY (Speagle 2020; Koposov et al. 2023), a package for dynamic nested sampling (Higson et al. 2019).

We choose the model with constant $T_{\rm eff}$ and $\log\tau$, variable $\log F$, and oxygen-rich dust composition as the baseline model for comparison. The best-fitting model has a temperature of $T_{\rm eff} = 3488 \pm 39$ K and a phase-averaged bolometric luminosity of $\log(L/{\rm L}_\odot) = 5.15 \pm 0.02$ (including the uncertainty in the host galaxy distance), placing the star at the luminous side of the SN II progenitors population (Fig. 4, left). The best-fitting luminosity and temperature imply a stellar radius of $R_\star = (1.03 \pm 0.03) \times 10^3\,{\rm R}_\odot$ – a greater radius compared to some of the largest known SN II progenitors (e.g. $R_\star \sim 740\,{\rm R}_\odot$ in Soumagnac et al. 2020). The progenitor bolometric luminosity varies with an amplitude of $\Delta\log(L/{\rm L}_\odot) = 0.13 \pm 0.01$ (i.e. 30 ± 1 per cent variation around the mean, or a peak-to-valley ratio of 1.82) over a period of $P = 1144.7 \pm 4.8$ d. This indicates a factor of 1.35 ± 0.02 change in the stellar radius from minimum to peak, assuming a constant $T_{\rm eff}$. At the time of the explosion (85.8 ± 1.1 d after the last maximum), the progenitor luminosity is $\log(L/{\rm L}_\odot) \sim 5.27$, with a radius of $R_\star \sim 1.18 \times 10^3\,{\rm R}_\odot$.

Based on the MIST stellar evolution tracks (Choi et al. 2016), the best-fitting values and error ellipse of $T_{\rm eff}$ and $\log(L/{\rm L}_\odot)$ correspond to a solar-metallicity, post-main-sequence star of $18.2^{+1.3}_{-0.6}\,{\rm M}_\odot$ (ZAMS mass, and hereafter), at the massive end of the SN II progenitor population. Alternatively, the Geneva model (Ekström et al. 2012) predicts that a solar-metallicity star of either 15 or $20\,{\rm M}_\odot$ can match the best-fitting $T_{\rm eff}$ and $\log(L/{\rm L}_\odot)$, but we cannot identify the best mass due to the sparsity of the model grid; the BPASS single-star model (Eldridge et al. 2017) shows that a star of $16\,{\rm M}_\odot$ would be the best match. We note that the mass estimate varies primarily due to model uncertainties, yet its luminosity already robustly places it at the brightest end of SN II progenitors.

The best-fitting optical depth of the dust envelope is $\tau = 2.92 \pm 0.02$ for the baseline model, which translates to an optical-band extinction of $A_{\rm V} = 8.43 \pm 0.11$ mag, assuming the Fitzpatrick (1999) extinction law for $R_V = 3.1$. Such a circumstellar dust extinction is extremely heavy; only two RSGs (LI-LMC 4 and WOH G 64) in the sample of Beasor & Smith (2022) has a comparably high $A_{\rm V}$. Assuming the opacity in Villaume et al. (2015), a gas-to-dust mass ratio of $\delta = 200$ for solar-metallicity giants (e.g. van Loon et al. 2005; Mauron & Josselin 2011), and a speed of $v_{\rm wind} = 50\,{\rm km\,s}^{-1}$ for dust-driven wind, the optical depth indicates a mass-loss rate of $\dot{M} = (4.32 \pm 0.26) \times 10^{-4}\,{\rm M}_\odot\,{\rm yr}^{-1}$. Such a mass-loss rate is substantially higher than the empirical mass-loss rates of stars with similar $\log(L/{\rm L}_\odot)$ and $T_{\rm eff}$, for ex-

---

[4] We assume a solar-metallicity progenitor here, but there is tentative evidence for a subsolar metallicity near the SN site ($\sim 0.7\,{\rm Z}_\odot$; Niu et al. 2023; Van Dyk et al. 2024; Zimmerman et al. 2024).

[5] http://svo2.cab.inta-csic.es/theory/fps/

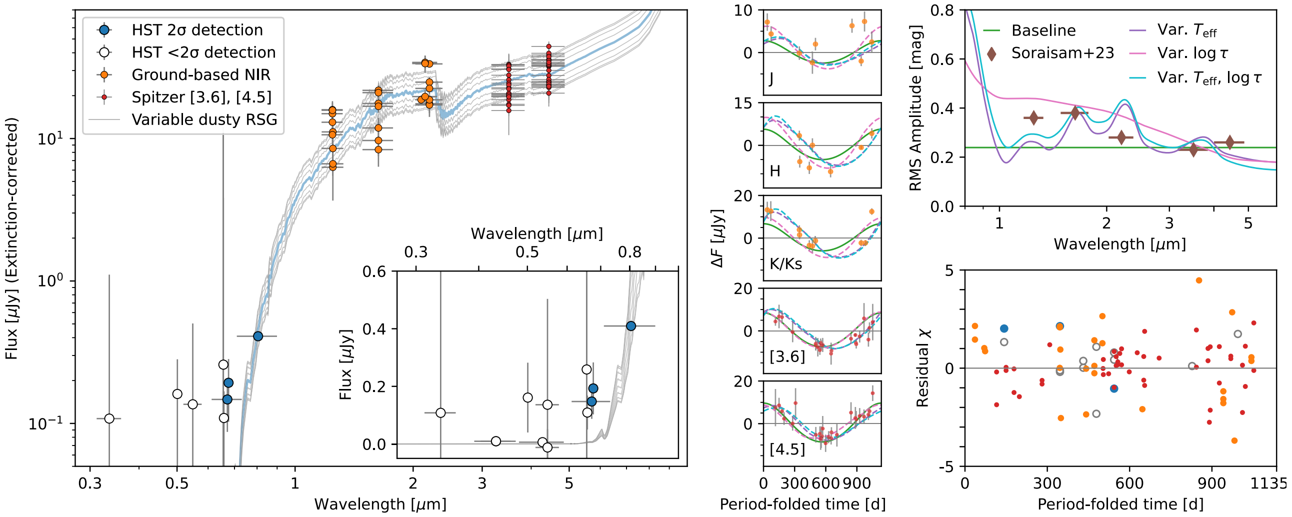

Figure 3. Modelling the observed SED with a variable dusty RSG model. The left panel shows *HST* optical and literature-compiled infrared photometry (data points), with Galactic and host extinction corrections applied. The central dark line represents the phase-averaged best-fitting baseline model, assuming a variable $\log(L/\mathrm{L}_\odot)$, but constant $T_{\rm eff}$ and $\log\tau$; the range of variation is indicated by light-colored lines. The inset panel shows the optical part on a linear scale. The middle panel shows the mean-subtracted and period-folded flux densities (data points) and the predictions of our baseline and alternative models (curves, the same legend as in the upper right panel). The upper right panel shows the predicted amplitude–wavelength relationship of the baseline and alternative models (Section 3.3), compared to the amplitude measured in S23. Alternative models with variation of $\log\tau$ (or $T_{\rm eff}$ and $\log\tau$) better reproduce the observed increase of amplitude towards shorter wavelengths. Finally, the lower right panel shows the residual error (model-observation difference, normalized by errors) for the baseline model fit (left panel), as a function of period-folded time, following the same symbols as in the left panel.

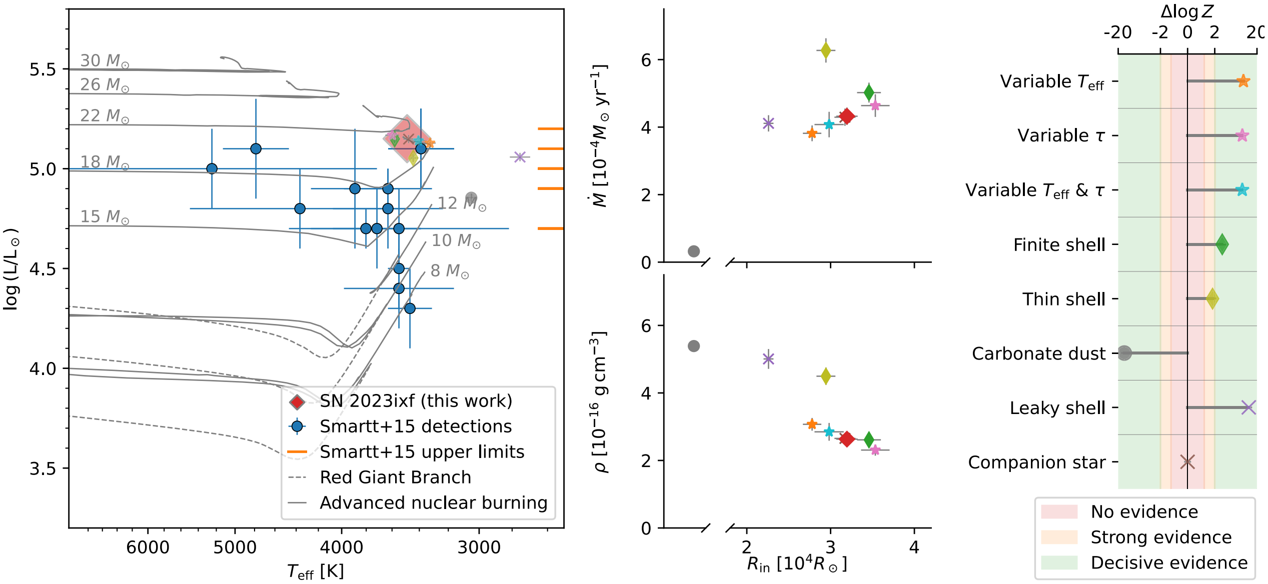

Figure 4. The progenitor properties of SN 2023ixf predicted by our baseline and alternative models. The left panel shows $T_{\rm eff}$ and $\log(L/\mathrm{L}_\odot)$ of the best-fitting baseline model (large diamond-shaped symbol) and alternative models (the same symbols as in the right panel), compared to the SN II progenitors summarized in Smartt (2015). MIST stellar evolution tracks (Choi et al. 2016) of different ZAMS masses are overlaid for comparison. The middle panel shows the inner radius of the dust envelope ($R_{\rm in}$), the mass loss rate ($\dot{M}$, upper), and the average CSM density inside $R_{\rm in}$ (ρ, lower) of the progenitor, derived from the baseline and alternative models, using the same symbols as in the right panel. Finally, the right panel shows the increase of Bayesian evidence ($\log Z$) for alternative models compared to the baseline model (with symmetric logarithmic axis); a positive $\Delta\log Z$ indicates that the alternative model is favored over the baseline model, whereas a negative $\Delta\log Z$ indicates that the alternative model underperforms compared to the baseline model.

ample, $[1.02 \pm 0.06\,(\mathrm{stat.})\,^{+2.29}_{-0.72}(\mathrm{sys.})] \times 10^{-5}\,\mathrm{M}_\odot\,\mathrm{yr}^{-1}$ assuming the Nieuwenhuijzen & de Jager (1990) relationship for general stars, or $[3.69 \pm 0.08\,(\mathrm{stat.})^{+3.72}_{-1.86}(\mathrm{sys.})] \times 10^{-5}\,\mathrm{M}_\odot\,\mathrm{yr}^{-1}$ assuming the van Loon et al. (2005) relationship for dusty RSGs and asymptotic giant branch (AGB) stars. However, it is in line with the period-dependent empirical mass-loss rate in Goldman et al. (2017) for AGB stars and RSGs ($[2.13 \pm 0.95\,(\mathrm{stat.})^{+5.67}_{-0.54}(\mathrm{sys.})] \times 10^{-4}\mathrm{M}_\odot\,\mathrm{yr}^{-1}$), given the large scatter of the relationship.

The luminosity and optical depth indicate a dust envelope inner radius of $R_{\rm in} = (3.20 \pm 0.13) \times 10^4\,{\rm R_\odot}$, within which the average CSM density is $\rho = (2.63 \pm 0.16) \times 10^{-16}\,{\rm g\,cm^{-3}}$, close to the estimate in Zimmerman et al. (2024) at the same radius in the extended wind region. Inside the radius of $R_{\rm p} = v_{\rm wind} P = 7.1 \times 10^3\,{\rm R_\odot}$, that is, the distance that stellar wind travels during one period of radial pulsation, or 'shell of pulsational mass loss', the average CSM density is $\rho = (5.25 \pm 0.31) \times 10^{-15}\,{\rm g\,cm^{-3}}$, also close to the extended wind density outside the shock breakout radius in Zimmerman et al. (2024). Notably, $R_{\rm p}$ is close to the radial extension of the confined CSM ($R_{\rm CSM}$) traced by the vanishing narrow emission lines. Assuming a shock velocity of $v_{\rm s} = 10^4\,{\rm km\,s^{-1}}$ and a time-scale of 5 d for the observed narrow emission lines, that is, the time that the shock propagates within the dense CSM where efficient Compton cooling produces the ionizing radiation in extreme ultraviolet, the CSM radius is at most $R_{\rm CSM} \simeq 6.2 \times 10^3\,{\rm R_\odot}$. The coincidence of $R_{\rm CSM}$ and $R_{\rm p}$ implies that the dense, confined CSM is ejected during, but not necessarily driven by, the final episode of radial pulsation. The CSM radius in Zimmerman et al. (2024) is $2.9 \times 10^3\,{\rm R_\odot}$, about half the simple estimate with $v_{\rm s}$ above. As the progenitor exploded near its peak luminosity, the dense CSM may have been ejected around the minimum, about half a period before the explosion. However, the complex structure of the shocked region and the increasing light crossing time introduce uncertainties in the shock propagation time in the dense CSM. The wind and shock speed also bear uncertainties (e.g. $v_{\rm wind} = 115\,{\rm km\,s^{-1}}$ in Smith et al. 2023). Therefore, $R_{\rm CSM}$ and $R_{\rm p}$ could differ by up to a factor of few. Moreover, the estimated CSM density based on post-explosion observations indicates a substantially higher $\dot{M}$ compared to estimates from progenitor properties ($\sim 10^{-2}\,{\rm M_\odot\,yr^{-1}}$ in Hiramatsu et al. 2023; Jacobson-Galán et al. 2023; Zimmerman et al. 2024), even higher than the typical mass-loss rates under the 'superwind' scenario (e.g. Förster et al. 2018), which requires a different mass-loss mechanism than dust-driven and pulsation-enhanced stellar winds.

We then compare the baseline model with a series of alternative models to illustrate the impact of different model choices on our results, and to determine whether other models provide better fits than the baseline model. The goodness-of-fit is primarily assessed by the improvement in Bayesian evidence ($\Delta \log Z$, i.e. the Bayes factor across two models), where a positive $\Delta \log Z$ indicates a more favorable model compared to the baseline model, given the existing data set, while a negative $\Delta \log Z$ indicates that the alternative model underperforms compared to the baseline model. To calculate $\log Z$ efficiently, the period of variation is fixed at $P = 1144.7$ d for the comparison here. We choose a threshold of $\Delta \log Z = 2$ (Jeffreys 1939) for decisive evidence in favour of an alternative model (Fig. 4, right).

First, we consider the scenario in which the variation of luminosity is accompanied by the variation of $T_{\rm eff}$ or $\log \tau$ with the same period, characterized by their amplitudes and phase lags with respect to the variation of luminosity. We find that either a periodic change in $T_{\rm eff}$ (with an amplitude of $\Delta T_{\rm eff} = 689 \pm 53$ K and a phase lag of 325 ± 27 d, i.e. $T_{\rm eff}$ peaks about 0.3 periods after maximum light), or a change in the dust optical depth (with an amplitude of $\Delta \log \tau = 0.055 \pm 0.014$ and phase lag of 469 ± 22 d, about half a period after maximum light) is more favourable compared to the baseline model. Allowing both $T_{\rm eff}$ and $\log \tau$ to vary, this more complex model does not improve the goodness of fit than the models in which only one varies, with similar amplitudes and phase lags in $T_{\rm eff}$ and $\log \tau$ ($\Delta T_{\rm eff} = 750 \pm 74$ K with a phase lag of 296 ± 31 d, and $\Delta \log \tau = 0.013 \pm 0.008$ with a phase lag of 621 ± 89 d). These alternative models predict similar $\log(L/{\rm L_\odot})$, $T_{\rm eff}$, $R_{\rm in}$, and $\dot{M}$ as the baseline model (Fig. 4, left and middle).

We note that alternative models with a variable τ better reproduce the observed root mean square (RMS) amplitude–wavelength relationship in S23 (i.e. stronger variability towards shorter wavelengths) than the baseline model does (Fig. 3, upper right). Alternative models with variable $T_{\rm eff}$ could also reproduce such a relationship, at least compared to the baseline model. Therefore, the periodic variation of luminosity must be accompanied by the variation of either $T_{\rm eff}$ or $\log \tau$, if not both. Physically, this implies the change of stellar or dust properties and hence SED shape over the period. Since $R_{\rm in}$ is about 4 times greater than $R_{\rm p}$ and 25 times greater than $R_\star$, instead of seeing the production of fresh dust during radial pulsations, the change in τ is likely due to the sublimation and condensation of dust out to a greater distance following the change of stellar irradiance. The half-period phase lag in the variation of $\log \tau$ indicates that the dust column density (and hence mass) peaks when the progenitor shrinks to its minimum radius, while the one-third-period phase lag in the variation of $T_{\rm eff}$ implies that the rate of dust condensation peaks after $T_{\rm eff}$ begins to decrease. We also note that the interpretation here may require further evidence, for example, from observations of Galactic RSGs.

Second, we consider the scenario in which the dust envelope has a finite radial extent, characterized by the ratio of outer to inner radius ($Y = R_{\rm out}/R_{\rm in}$). Besides the baseline model which has a very extended, 'infinite' dust envelope ($Y = 10^3$), we consider the case of a finite ($Y = 10$) and a thin ($Y = 2$) dust shell. We find that these models improve the goodness of fit in general ($\Delta \log Z = 3.07$ for $Y = 10$; and $\Delta \log Z = 1.75$ for $Y = 2$), similar to the conclusions drawn by Kilpatrick & Foley (2018) for the progenitor of SN 2017eaw. It should be emphasized that the dust optical depth is mainly sensitive to the column density integrated along the line of sight. Although the radial distribution of the dust has an effect on the radiative transfer and thus the observed SED, the pre-explosion data set here may have limited constraining power in distinguishing a finite-radius envelope from an extended envelope model. It is also possible that neither an extended envelope nor a confined dust shell accurately represents the dust distribution in reality.

Third, the circumstellar dust of RSGs are mainly oxygen-rich silicates, but here we consider an alternative model with a carbon-rich composition. We find that using carbonate dust degrades the quality of fit ($\Delta Z = -14.5$) compared to the oxygen-rich baseline model, in contrast to the conclusions in Kilpatrick & Foley (2018) for SN 2017eaw and Niu et al. (2023) for SN 2023ixf. Meanwhile, the carbonate dust model leads to a significantly cooler and lower luminosity progenitor, beyond the coverage of MIST isochrones (Fig. 4, left). The implied dust envelope inner radius and mass-loss rate are also lower than models based on oxygen-rich silicate dust (Fig. 4, middle). We conclude that using carbonate dust does not improve the model fit and may result in biased and even unphysical progenitor properties. This finding aligns with observations of Galactic RSGs, where a carbon-rich dust model is considered a less likely scenario (Verhoelst et al. 2009; see also the discussion in the context of SN II progenitors in Van Dyk et al. 2024).

Fourth, the CSM around the progenitor is likely asymmetric (Smith et al. 2023; Vasylyev et al. 2023). Therefore, the progenitor could be partially or non-uniformly obscured by the circumstellar dust. We consider the case in which a fraction of the progenitor's light has escaped without being absorbed and re-emitted by the dust. The best-fitting escape fraction of this 'leaky shell' model is $f_{\rm esc} =$

21.5 ± 1.6 per cent, with an increase in the Bayesian evidence of $\Delta \log Z = 12.9$, indicating that either non-spherical or clumpy dust could better fit the observed SED. However, the model prefers a much cooler star compared to the baseline model ($T_{\rm eff} = 2754 \pm 59$ K). Despite the improvement in $\Delta \log Z$, we note that the wavelength coverage of our data set might not be able to constrain the dust geometry effectively.

Finally, we consider the potential contribution of an unobscured binary companion star in the observed SED. Assuming that the companion star lies on the same best-matching MIST isochrone as the progenitor, we use the companion ZAMS mass (M_2) as the free parameter with a flat prior. We add a new SED component based on the BASEL v3.1 stellar template (Lejeune, Cuisinier & Buser 1997) using the effective temperature and luminosity predicted from the isochrone. The best-fitting model has $M_2 = 4.3 \pm 1.5\,{\rm M}_\odot$, close to a main-sequence star with $T_{\rm eff,2} = (1.55 \pm 0.33) \times 10^4$ K and $\log(L_2/{\rm L}_\odot) = 2.49 \pm 0.58$. The single-sided 95 per cent upper limit is $5.6\,{\rm M}_\odot$, or $\log(L_2/{\rm L}_\odot) = 2.92$ in luminosity. The companion star model does not outperform the baseline model ($\Delta \log Z = 0.0$). Nevertheless, the sensitivity limit of our data may not confirm the single-star nature of the progenitor; only companions of $M_2 > 5.6\,{\rm M}_\odot$ can be robustly ruled out. We also note that assuming an unobscured companion star here may be an oversimplification. The inner radius of the dust envelope is greater than the separation observed in some close binaries. Therefore, it is possible that the binary companion star suffers from a comparable level of dust obscuration as the primary. In such a case, a more massive and luminous companion star could be allowed.

In Table 2, we summarize the progenitor properties in earlier works and our results. We derive consistent $\log(L/{\rm L}_\odot)$ and M values compared to other works, except for K23, which prefers a lower luminosity and hence a lower mass progenitor. S23 estimated a marginally higher luminosity based on the period–luminosity relationship in Soraisam et al. (2018); nevertheless, the estimated ZAMS mass is consistent with our result. The effective temperature is not robustly constrained in general; we find a $T_{\rm eff}$ that is consistent with earlier works but cooler than K23. Furthermore, we find a comparable dust optical depth (or extinction) with Van Dyk et al. (2024) but higher than other works. A higher τ value, along with the larger $R_{\rm in}$ (e.g. compared to $8600\,{\rm R}_\odot$ in K23), a dust temperature-sensitive property, leads to a higher $\dot{M}$. Notably, the analyses in J23 and Van Dyk et al. (2024) are based on the Grid of RSG and AGB ModelS (GRAMS; Sargent, Srinivasan & Meixner 2011; Srinivasan, Sargent & Meixner 2011), while the key results are not systematically different than works using MARCS and DUSTY for SED modelling. The variance across these independent analyses is attributable to the different subsets of archival data used, the various methodologies for photometry, the choice of stellar and dust SED models, and perhaps most importantly, the interpretation of results based on stellar evolution models or empirical relationships. For example, if we use the IRAC measurement from S23 instead, the progenitor luminosity increases by 0.08 dex, a significant change compared to the systematic error from SED fitting alone (0.01 dex). This highlights the challenges and possible systematic biases in analysing and interpreting the pre-explosion data set.

4 SUMMARY AND DISCUSSION

We identify the progenitor star of SN 2023ixf in the pre-explosion *HST*/ACS image using Keck/NIRC2 adaptive optics imaging. The SN position, precisely determined to a total uncertainty of 19.5 mas, unambiguously coincides with a red source in the *HST*/ACS image; other sources, including a nearby source detected using iteratively subtracted PSF photometry, are ruled out. With forced PSF photometry, we obtain 2σ detections of the progenitor in three *HST* bands.

Given the reported infrared excess and variability of the progenitor, we fit the SED of a dusty variable RSG to a combined data set including our *HST* photometry and infrared measurements in the literature. We find $\log(L/{\rm L}_\odot) = 5.15 \pm 0.02$ and $T_{\rm eff} = 3488 \pm 39$ K for the best-fitting model, consistent with a post-main-sequence massive single star of $18.2^{+1.3}_{-0.6}\,{\rm M}_\odot$, among the most luminous and massive SN II progenitors. The heavy dust obscuration ($\tau = 2.92 \pm 0.02$ at 1 μm) indicates an enhanced pre-SN mass-loss rate of $(4.32 \pm 0.26) \times 10^{-4}\,{\rm M}_\odot\,{\rm yr}^{-1}$ and a CSM density of $(5.25 \pm 0.31) \times 10^{-15}\,{\rm g\,cm}^{-3}$ inside the shell of pulsational mass loss. Based on the time-scale of the observed narrow emission lines and the period of progenitor variability, we suggest that the dense and confined CSM is ejected during the last episode of radial pulsation before the explosion.

Table 2. Key progenitor properties compared to other works.

	$\log(L/{\rm L}_\odot)$	$T_{\rm eff}$ (K)	M (${\rm M}_\odot$)	τ (1μm)	$A_{\rm V}$ (mag)	$\dot{M}$ ($10^{-4}{\rm M}_\odot$ yr^{-1})	SED model
Jencson et al. (2023)	5.1 ± 0.2	3500^{+800}_{-1400}	17 ± 4	2.2	–	1.5–15[a]	Mainly GRAMS
Kilpatrick et al. (2023)	4.74 ± 0.07	3920^{+200}_{-160}	~ 11	–	4.6 ± 0.2	0.026 ± 0.002[a]	MARCS + DUSTY
Niu et al. (2023)	5.11 ± 0.08	3700[b]	16.2–17.4	–	$6.94^{+0.63}_{-0.64}$	~ 0.43[a]	MARCS + DUSTY
Pledger & Shara (2023)	–	–	8–10[c]	–	–	–	–
Soraisam et al. (2023)	5.27 ± 0.12	3200[b]	20 ± 4	–	–	2–4[d]	–
. . .	5.37 ± 0.12	3500[b]	. . .	–	–	. . .	–
Van Dyk et al. (2024)	$4.95^{+0.08}_{-0.07}$	2770^{+380}_{-430}	12–14	$1.7^{+0.3}_{-0.2}$[e]	–	$0.12^{+0.14}_{-0.04}$[e,f]	GRAMS
Xiang et al. (2024)	4.83	3091^{+422}_{-258}	12^{+2}_{-1}	–	$6.79^{+1.86}_{-0.92}$	0.06–0.09	MARCS + DUSTY
This work	5.15 ± 0.02	3488 ± 39	$18.2^{+1.3}_{-0.6}$	2.92 ± 0.02	8.43 ± 0.11	4.32 ± 0.26	MARCS + DUSTY

Notes. [a] Scaled to $v_{\rm wind} = 50{\rm km\,s}^{-1}$ and $\delta = 200$ as assumed in this work.
[b] Fixed parameter. [c] Based on the best-matching isochrone in the colour–magnitude diagram.
[d] Inferred from period and luminosity (Goldman et al. 2017) assuming $\delta = 200$.
[e] Based on the median value and 16th, 84th percentiles. [f] Converted from the dust production rate assuming $\delta = 200$.

We find strong evidence for the synchronized variation of dust or stellar properties along with the variation of luminosity. Specifically, alternative models with a variable dust optical depth better reproduce the observed amplitude–wavelength relationship. We suggest that the luminosity variation and radial pulsation of the progenitor may lead to periodic dust sublimation and condensation, and hence the change in τ, near the inner radius of the dust envelope. However, the change in other dust properties (e.g. temperature and grain size) could also lead to the apparent variability of τ.

Furthermore, non-spherical dust geometry or partial dust obscuration remains possible; about 21.5 ± 1.6 per cent of the progenitor's light may have escaped without being reprocessed by the circumstellar dust envelope. However, any unobscured companion star above $5.6\,\mathrm{M}_\odot$ can be ruled out based on the data set.

We conclude that the progenitor of SN 2023ixf is among the most massive, luminous, and heavily obscured SN II progenitors, which likely experienced enhanced mass loss before the explosion.

ACKNOWLEDGEMENTS

The authors would like to thank Jacob Jencson for kindly providing his *Spitzer*/IRAC and MMIRS measurements before the acceptance of Jencson et al. (2023). The authors would also like to thank Ping Chen, Ningchen Sun, and Subo Dong for their valuable comments on this work. YQ thanks Jianwei Lyu and Fengwu Sun for the discussion on infrared flux calibration, and Lile Wang for the discussion on circumstellar dust thermodynamics. YQ thanks Weidong Li (deceased), whose work on the progenitor of SN 2011fe in Messier 101 (Li et al. 2011b) motivated his career as an astrophysicist.

AGY's research is supported by the EU via ERC grant no. 725161, the ISF GW excellence centre, an IMOS space infrastructure grant and BSF/Transformative and GIF grants, as well as the André Deloro Institute for Advanced Research in Space and Optics, The Helen Kimmel Center for Planetary Science, the Schwartz/Reisman Collaborative Science Program and the Norman E Alexander Family M Foundation ULTRASAT Data Center Fund, Minerva and Yeda-Sela; AGY is the incumbent of the The Arlyn Imberman Professorial Chair. MWC acknowledges support from the National Science Foundation with grant nos PHY-2010970 and OAC-2117997.

SS acknowledges support from the G.R.E.A.T. research environment, funded by *Vetenskapsrådet*, the Swedish Research Council, project number 2016–06012.

DATA AVAILABILITY

The compiled photometric data set, photometry program, SED model grid, and the best-fitting result are available upon reasonable request.

REFERENCES

Anderson J., King I. R., 2000, PASP, 112, 1360
Anderson J., King I. R., 2006, PSFs, Photometry, and Astronomy for the ACS/WFC, Instrument Science Report ACS 2006–01, 34 pp.
Beasor E. R., Davies B., 2016, MNRAS, 463, 1269
Beasor E. R., Smith N., 2022, ApJ, 933, 41
Bellini A., Anderson J., Grogin N. A., 2018, Focus-diverse, empirical PSF models for the ACS/WFC, Instrument Science Report ACS 2018–8
Berger E. et al., 2023, ApJ, 951, L31
Bianciardi G. et al., 2023, Transient Name Server AstroNote, 213, 1
Bostroem K. A. et al., 2023, ApJ, 956, L5
Bradley L. et al., 2022, astropy/photutils: 1.5.0, Zenodo, https://doi.org/10.5281/zenodo.6825092
Chandra P., Chevalier R. A., Maeda K., Ray A. K., Nayana A. J., 2024, ApJ, 963, L4
Choi J., Dotter A., Conroy C., Cantiello M., Paxton B., Johnson B. D., 2016, ApJ, 823, 102
Davies B., Beasor E. R., 2018, MNRAS, 474, 2116
Davies B., Beasor E. R., 2020, MNRAS, 493, 468
Dong Y. et al., 2023, ApJ, 957, 28
Ekström S. et al., 2012, A&A, 537, A146
Eldridge J. J., Stanway E. R., Xiao L., McClelland L. A. S., Taylor G., Ng M., Greis S. M. L., Bray J. C., 2017, Publ. Astron. Soc. Aust., 34, e058
Fitzpatrick E. L., 1999, PASP, 111, 63
Flinner N., Tucker M. A., Beacom J. F., Shappee B. J., 2023, Res. Notes Am. Astronom. Soc., 7, 174
Foreman-Mackey D., Hogg D. W., Lang D., Goodman J., 2013, PASP, 125, 306
Förster F. et al., 2018, Nat. Astron., 2, 808
Gaia Collaboration, 2018, A&A, 616, A1
Goldman S. R. et al., 2017, MNRAS, 465, 403
Grefenstette B. W., Brightman M., Earnshaw H. P., Harrison F. A., Margutti R., 2023, ApJ, 952, L3
Guetta D., Langella A., Gagliardini S., Della Valle M., 2023, ApJ, 955, L9
Gustafsson B., Edvardsson B., Eriksson K., Jørgensen U. G., Nordlund Å., Plez B., 2008, A&A, 486, 951
Higson E., Handley W., Hobson M., Lasenby A., 2019, Stat. Comput., 29, 891
Hiramatsu D. et al., 2023, ApJ, 955, L8
Horiuchi S., Nakamura K., Takiwaki T., Kotake K., Tanaka M., 2014, MNRAS, 445, L99
Hosseinzadeh G. et al., 2023, ApJ, 953, L16
Itagaki K., 2023, Transient Name Server Discovery Rep., 2023-1158, 1
Ivezic Z., Elitzur M., 1997, MNRAS, 287, 799
Jacobson-Galán W. V. et al., 2023, ApJ, 954, L42
Jeffreys H., 1939, Theory of Probability. Oxford University Press, Oxford
Jencson J. E. et al., 2023, ApJ, 952, L30
Kilpatrick C. D. et al., 2023, ApJ, 952, L23
Kilpatrick C. D., Foley R. J., 2018, MNRAS, 481, 2536
Koposov S. et al., 2023, joshspeagle/dynesty: v2.1.2, Zenodo, https://doi.org/10.5281/zenodo.7995596
Lejeune T., Cuisinier F., Buser R., 1997, A&AS, 125, 229
Li G. et al., 2024, Nature, 627, 754
Li W. et al., 2011a, MNRAS, 412, 1441
Li W. et al., 2011b, Nature, 480, 348
Mao Y. et al., 2023, Transient Name Server AstroNote, 130, 1
Mauron N., Josselin E., 2011, A&A, 526, A156
Neustadt J. M. M., Kochanek C. S., Smith M. R., 2024, MNRAS, 527, 5366
Nieuwenhuijzen H., de Jager C., 1990, A&A, 231, 134
Niu Z., Sun N.-C., Maund J. R., Zhang Y., Zhao R., Liu J., 2023, ApJ, 955, L15
O'Connor E., Ott C. D., 2011, ApJ, 730, 70
Panjkov S., Auchettl K., Shappee B. J., Do A., Lopez L. A., Beacom J. F., 2023, preprint (arXiv:2308.13101)
Perley D. A., Gal-Yam A., Irani I., Zimmerman E., 2023, Transient Name Server AstroNote, 119, 1
Pledger J. L., Shara M. M., 2023, ApJ, 953, L14
Ransome C. L. et al., 2024, ApJ, 965, 93
Ravensburg E., Carenza P., Eckner C., Goobar A., 2024, Phys. Rev. D, 109, 023018
Riess A. G. et al., 2022, ApJ, 934, L7
Sargent B. A., Srinivasan S., Meixner M., 2011, ApJ, 728, 93
Sarmah P., 2024, J. Cosmol. Astropart. Phys., 2024, 083
Schlafly E. F., Finkbeiner D. P., 2011, ApJ, 737, 103
Schlegel D. J., Finkbeiner D. P., Davis M., 1998, ApJ, 500, 525
Sgro L. A. et al., 2023, Res. Notes Am. Astron. Soc., 7, 141
Shivvers I. et al., 2017, PASP, 129, 054201

Skrutskie M. F. et al., 2006, AJ, 131, 1163
Smartt S. J., 2009, ARA&A, 47, 63
Smartt S. J., 2015, Publ. Astron. Soc. Aust., 32, e016
Smith N., Pearson J., Sand D. J., Ilyin I., Bostroem K. A., Hosseinzadeh G., Shrestha M., 2023, ApJ, 956, 46
Soraisam M. D. et al., 2018, ApJ, 859, 73
Soraisam M. D. et al., 2023, ApJ, 957, 64
Soumagnac M. T. et al., 2020, ApJ, 902, 6
Speagle J. S., 2020, MNRAS, 493, 3132
Srinivasan S., Sargent B. A., Meixner M., 2011, A&A, 532, A54
Teja R. S. et al., 2023, ApJ, 954, L12
Van Dyk S. D. et al., 2023, MNRAS, 519, 471
Van Dyk S. D. et al., 2024, ApJ, 968, 27
Van Dyk S. D., 2017, Philos. Trans. R. Soc. Lond. Ser. A, 375, 20160277
van Loon J. T., Cioni M. R. L., Zijlstra A. A., Loup C., 2005, A&A, 438, 273
Vasylyev S. S. et al., 2023, ApJ, 955, L37
Verhoelst T., van der Zypen N., Hony S., Decin L., Cami J., Eriksson K., 2009, A&A, 498, 127
Villaume A., Conroy C., Johnson B. D., 2015, ApJ, 806, 82
Walmswell J. J., Eldridge J. J., 2012, MNRAS, 419, 2054
Xiang D., Mo J., Wang L., Wang X., Zhang J., Lin H., Wang L., 2024, Sci. China Phys. Mech. Astron., 67, 219514
Yamanaka M., Fujii M., Nagayama T., 2023, PASJ, 75, L27
Yaron O., Bruch R., Chen P., Irani I., Zimmerman E., Gal-Yam A., Qin Y., 2023, Transient Name Server AstroNote, 133, 1
Yoon S.-C., Cantiello M., 2010, ApJ, 717, L62
Zimmerman E. A. et al., 2024, Nature, 627, 759

This paper has been typeset from a TEX/LATEX file prepared by the author.